Analytical Method for Magnetic Field Calculation in a Low-Speed Permanent-Magnet Harmonic Machine

Linni Jian, *Member, IEEE*, Guoqing Xu, Chunting Chris Mi, *Senior Member, IEEE*, K. T. Chau, *Senior Member, IEEE*, and C. C.Chan, *Fellow, IEEE*

***Abstract*—Magnetic-gearing effect has become increasingly attractive when designing direct-drive low-speed permanent-magnet machines. The machines derived from the magnetic-gearing effect can be termed as harmonic machines. Unlike the conventional types, harmonic machines rely on the field harmonics to achieve energy conversion and transmission. The detailed knowledge of the field distributions in the air gap is vitally important for predicting and optimizing its performance. In this paper, we present an analytical approach to calculate the magnetic field distribution in a low-speed permanent-magnet harmonic machine. A series-slot model which is composed of a group of partial differential equations concerning the scalar magnetic potential is built up. Then, the field solutions are obtained by using the method of separating variables and analyzing the field boundary conditions. Finally, the flux densities are derived from the scalar magnetic potentials. All the results agree well with those obtained from the finite element method.**

***Index Terms*—Analytical calculation, direct drive, harmonic machine, low speed, magnetic gearing, permanent magnet.**

I. Introduction

LOW-SPEED permanent-magnet (PM) machines have attracted increasing attention in several occasions, such as wind power generation, electric vehicles, electric vessels, home appliances, etc., since they can offer the so-called direct-drive operation which is the benefit for avoiding the nuisances caused by mechanical gearboxes. In order to result in relatively low-rated speed, multipolar PMs are usually adopted. In [1], a 48-pole 144-slot outer-rotor surface-mounted PM generator was proposed for directly coupled wind turbines. A comparative study showed that it possesses several attractive merits, such as compact structure, light weight, and high efficiency [2]. In [3], a 24-pole 72-slot axial-flux PM motor was presented for a machine-room-less elevator system. In order to improve torque density, a 30-pole 60-slot double-rotor axial-flux PM motor was proposed for electric vehicles [4]. In these machines, distributed windings were employed, which result in enormous slot numbers. This will definitely cause problems, such as deep saturation [5], high temperature rise [6], and so on. By adopting fractional slot and concentrated windings [7]–[9], these shortcomings can be alleviated. Moreover, it can reduce the volume of the coil end, decrease the copper loss, and improve the flux-weakening operation ability [10]. Although there are differences on the winding structure and the field path, all the aforementioned machines rely on the fundamental component of the electromagnetic field to realize electromechanical energy conversion.

Recently, the magnetic-gearing effect has become more and more attractive when designing low-speed PM machines [11], [12]. Coaxial magnetic gears [13], [14] rely on the field modulation arising from the noneven magnetic field path to excite abundant asynchronous harmonic components. With the interaction of specific harmonics [15], both torque transmission and speed variation can be achieved. In [16], a magnetic-geared machine was proposed for wind power generation, in which a PM high-speed brushless machine was artfully integrated into a coaxial magnetic gear to realize low-speed operation. Moreover, it can offer very large torque density due to the torque amplification aroused by the magnetic gear. Then, a flux-modulated machine was proposed [17], in which, the high-speed rotor adopted in the magnetic-geared machine was removed in order to simplify the overall structure. Thus, the asynchronous field harmonics are directly involved into the electromechanical energy conversion process. Although the field harmonics are usually weaker than the field fundamental component, quantitative comparison showed that this machine can provide higher torque density than its conventional counterparts [18]. In [19], the field modulation is achieved by directly equipping flux-modulation poles on the stator. Thus, only one air gap is needed. Calculation results showed that it can further improve the torque density. Unlike the conventional machines, these newly emerging types rely on the field harmonics to achieve energy conversion and transmission. Thus, they can be termed as harmonic machines in general.

As is well known that the detailed knowledge of the magnetic field distribution in air gap is vitally important for design and optimization of PM machines, especially for low-speed PM harmonic machines. Although numerical tools, such as finite element method (FEM), are able to offer precisely field prediction, they can provide neither closed-form solution nor physical insight. In recent years, much progress has been made

Manuscript received October 7, 2010; revised December 3, 2010; accepted March 30, 2011. Date of publication May 10, 2011; date of current version August 19, 2011. Paper no. TEC-00392-2010

L. Jian is with the Shenzhen Institutes of Advanced Technology, Chinese Academy of Sciences, Shenzhen 518055, China (e-mail: ln.jian@siat.ac.cn).

G. Xu is with the The Chinese University of Hong Kong, Shatin, Hong Kong, and also with the Department of Electrical Engineering, Tongji University, Shanghai, China (e-mail: gqxu@mae.cuhk.edu.hk).

C. C. Mi is with the Department of Electrical and Computer Engineering, University of Michigan-Dearborn, Dearborn, MI 48128 USA (e-mail: chrismi@umich.edu).

K. T. Chau and C. C. Chan are with Electrical and Electronic Engineering Department, The University of Hong Kong, Pokfulam, Hong Kong (e-mail: ktchau@eee.hku.hk; ccchan@eee.hku.hk).

Color versions of one or more of the figures in this paper are available online at http://ieeexplore.ieee.org.

Digital Object Identifier 10.1109/TEC.2011.2140373

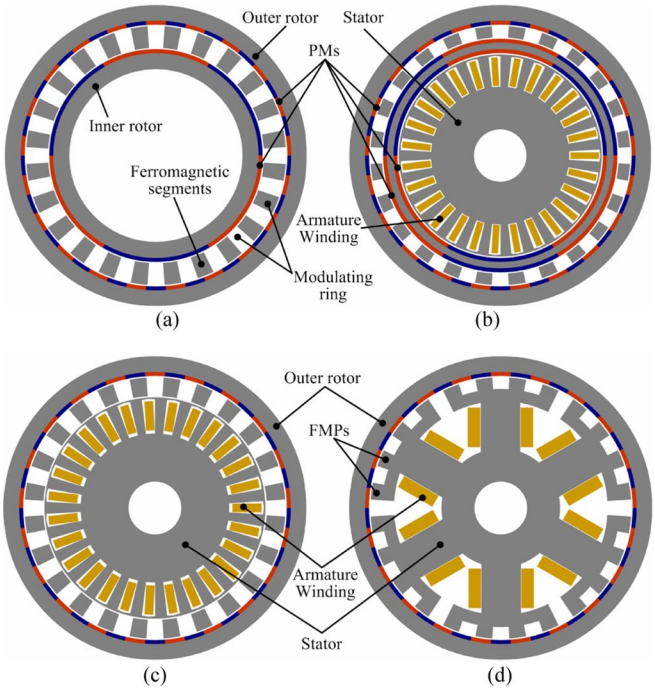

Fig. 1. Magnetic-gearing effect. (a) Coaxial magnetic gear. (b) Magnetic-geared machine. (c) Flux-modulated machine. (d) Harmonic machine.

in analytical modeling of PM machines. Generally, there are two sorts of analytical methods for calculating magnetic field distribution in PM machines: one is based on conformal transformation [20]–[22], while the other is based on Fourier series decomposition [23]–[27]. The purpose of this paper is to propose an analytical method for magnetic field calculation in low-speed PM harmonic machines. Fourier series decomposition will be engaged to obtain the solutions of Laplace/Poisson equations that represent the field behavior in each calculation region. Moreover, a series-slot model will be employed to improve the calculation accuracy. The validity of the proposed analytical approach will be verified by comparing the calculation results with those obtained from the FEM.

II. PM Harmonic Machines

PM harmonic machines are derived from the magnetic-gearing effect. Fig. 1(a) shows the topology of a coaxial magnetic gear (CMG). It consists of two rotational parts: the inner rotor (high-speed rotor) and the outer rotor (low-speed rotor), and one stationary part: the modulating ring. PMs are employed on the two rotors. p_1 and p_2 denote the pole-pair numbers (PPN) of PMs on the outer rotor and the inner rotor, respectively. The modulating ring is composed of several ferromagnetic segments that are symmetrically deployed in the space between the two rotors. In order to enforce the structural strength for high-torque transmission, epoxy is filled in the slot area.

The modulating ring takes charge of modulating the magnetic fields in the two air gaps beside it. Denoted by N_s the number of ferromagnetic segments, the magnetic field in the both air gaps built up by the PMs on the two rotors consists of abundant harmonics, and the PPN of these harmonics can be expressed as

$$\mathrm{PPN}_{i,j,k} = |(2i-1)\,p_k + jN_s| \tag{1}$$

where $i = 1, 2, 3, ..., \infty$, $j = 0, \pm1, \pm2, \pm3, ..., \pm\infty$, $k = 1, 2$, and $k = 1$ implies that the harmonic component is excited by the outer rotor PMs, while $k = 2$ means that it is excited by the inner rotor PMs.

For each harmonic, the corresponding rotational speed can be given by

$$\omega_{i,j,k} = \frac{(2i-1)\,p_k}{(2i-1)\,p_k + jN_s}\omega_k \tag{2}$$

where ω_1 and ω_2 are the rotational speeds of the outer rotor and the inner rotor, respectively.

Stable torque transmission can be achieved between the two rotors, as long as it satisfies

$$N_s = p_1 + p_2 \tag{3}$$

and the rotational speeds of the two rotors are governed by

$$\omega_2 = -\frac{p_1}{p_2}\omega_1 = -G_r\omega_1 \tag{4}$$

where G_r is the so-called gear ratio. The minus sign indicates that the two rotors rotate in opposite directions.

Since all the PMs are involved into the torque transmission, the CMG can provide as high-torque density as its mechanical counterparts. Moreover, the noncontact torque transmission can avoid the nuisances existing in the mechanical gearboxes, such as friction loss, audible noise, mechanical vibration, and need of regular lubrication and maintenance. Fig. 1(b) shows the topology of the magnetic-geared machine. A PM high-speed brushless machine is artfully placed in the inner bore of the CMG, and shares its rotor with the CMG (inner rotor of the CMG). Although it can provide both very high torque density and low-speed operation, its mechanical structure is too complex: it consists of two rotational parts, two stationary parts, and three air gaps. Fig. 1(c) shows the topology of the flux-modulated machine. It can be seen that the inner rotor existing in Fig. 1(b) is removed, and the harmonics excited by the modulating ring directly interact with the armature windings to achieve electromechanical energy conversion. This machine can also provide low-speed operation, and it can offer higher torque density than the conventional PM machines. However, it is still composed of one rotational part, two stationary parts, and two air gaps. In order to further simplify the mechanical structure, as illustrated in Fig. 1(d), the ferromagnetic modulating poles (FMPs) are directly installed on the stator of the machine; thus, only one air gap is needed. Moreover, centralized armature windings are employed to improve air ventilation and heat dissipation, and reduce copper loss and manufacturing cost. Similar to the flux-modulated machine, this harmonic machine also replies on the field harmonics to achieve energy conversion and transmission. In what follows, the magnetic field distribution in it will be theoretically analyzed.

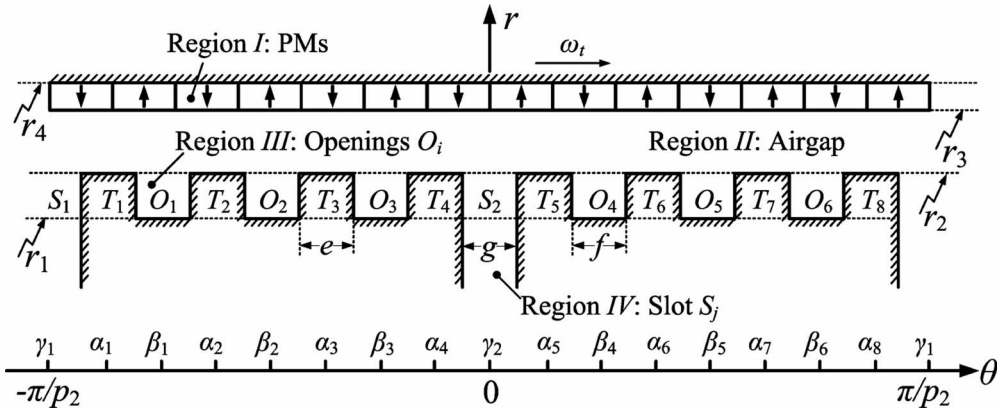

Fig. 2. Analytical model in a pseudopolar coordinate.

III. Analytical Model

In the harmonic machine shown in Fig. 1(d), the PPN of PMs on the outer rotor equals 24 ($p_1 = 21$), and the three-phase armature windings has six poles ($p_2 = 3$). Moreover, the number of FMPs is 24. Thus, the gear ratio of 7:1 is resulted. The series-slot model within a pole-pair pitch can be represented in the pseudopolar coordinate as shown in Fig. 2. The widths of the slots, openings, and FMPs are denoted by *g*, *f*, and *e*, respectively. r_1, r_2, r_3, and r_4 are the inside radius of the openings, outside radius of the FMPs, inside radius of the PMs, and outside radius of the PMs, respectively. The θ-axis coordinates of the central lines of the *k*th FMP T_k, *i*th opening O_i, and *j*th slot S_j are denoted by α_k, β_i, and γ_j, respectively. ω_t denotes the rotational speed of the outer rotor. Moreover, for simplicity, several assumptions should be made.

1) The permeabilities of the iron yokes are infinite.
2) The PMs have the same permeability with the airspace.
3) The depth of the slots is infinite.

The calculation region can be classified into four parts: PMs (Region I), air gap (Region II), openings between the FMPs (Region III), and slots (Region IV). In various regions, the flux density $\vec{B}$ and field intensity $\vec{H}$ are expressed as

$$\text{in Region I:} \quad \vec{B} = \mu_0 \mu_r \vec{H} + \mu_0 \vec{M} \tag{5}$$

$$\text{in Regions II, III, IV:} \quad \vec{B} = \mu_0 \vec{H} \tag{6}$$

where μ_r is the relative recoil permeability and $\vec{M}$ is the residual magnetization vector. By employing the scalar magnetic potential φ, the field behavior can be governed by a set of 2-rank partial differential equations (Laplace/Poisson equations)

$$\text{in Region I:} \quad \nabla^2 \varphi^I (r, \theta) = \frac{\operatorname{div}\left(\vec{M}\right)}{\mu_r} \tag{7}$$

$$\vec{M} = M_r \vec{r} + M_\theta \vec{\theta} \tag{8}$$

where $M_\theta = 0$ and $M_r = M_r(\theta_0, \omega_t, t)$ indicates the PM magnetization distribution shown in Fig. 3. By using Fourier series

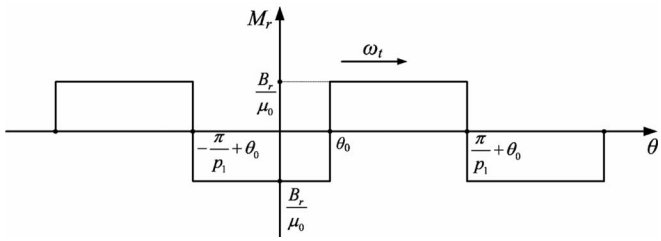

Fig. 3. PM magnetization distribution.

decomposition over $[-\pi, \pi]$, it yields

$$M_r = \sum_{m=1}^{\infty} Z_m \begin{bmatrix} \cos\left(mp_1\left(\theta_0 + \omega_t t\right)\right) \sin mp_1\theta \\ -\sin\left(mp_1\left(\theta_0 + \omega_t t\right)\right) \cos mp_1\theta \end{bmatrix} \tag{9}$$

$$Z_m = \frac{2\left[1 - (-1)^m\right] B_r}{m\pi\mu_0} \tag{10}$$

$$\text{in Region II:} \quad \nabla^2 \varphi^{\mathrm{II}} (r, \theta) = 0 \tag{11}$$

$$\text{in Region III:} \quad \nabla^2 \varphi^{\mathrm{III}} (r, \theta) = 0 \tag{12}$$

$$\text{in Region IV:} \quad \nabla^2 \varphi^{\mathrm{IV}} (r, \theta) = 0. \tag{13}$$

Then, the corresponding boundary conditions can be defined as following.

For the *i*th opening O_i, $i = 1, 2, ..., 6$

$$\theta_i^L = \beta_i - f/2 \text{ and } r \in [r_1, r_2] : \varphi_i^{\mathrm{III}}\left(r, \theta_i^L\right) = 0 \tag{14}$$

$$\theta_i^R = \beta_i + f/2 \text{ and } r \in [r_1, r_2] : \varphi_i^{\mathrm{III}}\left(r, \theta_i^R\right) = 0 \tag{15}$$

$$r = r_1 \text{ and } \theta \in [\theta_i^L, \theta_i^R] : \varphi_i^{\mathrm{III}}(r_1, \theta) = 0. \tag{16}$$

For the *j*th slot S_j, $j = 1, 2$

$$\theta_j^L = \gamma_j - g/2 \text{ and } r \in [0, r_2] : \varphi_j^{\mathrm{IV}}\left(r, \theta_j^L\right) = 0 \tag{17}$$

$$\theta_j^R = \gamma_j + g/2 \text{ and } r \in [0, r_2] : \varphi_j^{\mathrm{IV}}\left(r, \theta_j^R\right) = 0 \tag{18}$$

$$r = 0 \text{ and } \theta \in [\theta_j^L, \theta_j^R] : \varphi_j^{\mathrm{IV}}(0, \theta) = 0. \tag{19}$$

For the air gap

$$r = r_2 \text{ and } \theta \in [\alpha_k - e/2, \alpha_k + e/2], k = 1, 2, ..., 8 : \varphi^{\mathrm{II}}(r_2, \theta) = 0 \tag{20}$$

$r = r_2$ and $\theta \in [\beta_i - f/2, \beta_i + f/2]$, $i = 1, 2, ..., 6$:

$$\varphi^{\mathrm{II}}(r_2, \theta) = \varphi_i^{\mathrm{III}}(r_2, \theta) \tag{21}$$

$$\left.\frac{\partial \varphi^{\mathrm{II}}(r, \theta)}{\partial r}\right|_{r=r_2} = \left.\frac{\partial \varphi_i^{\mathrm{III}}(r, \theta)}{\partial r}\right|_{r=r_2} \tag{22}$$

$r = r_2$ and $\theta \in [\gamma_j - g/2, \gamma_j + g/2]$, $j = 1, 2$:

$$\varphi^{\mathrm{II}}(r_2, \theta) = \varphi_j^{\mathrm{IV}}(r_2, \theta) \tag{23}$$

$$\left.\frac{\partial \varphi^{\mathrm{II}}(r, \theta)}{\partial r}\right|_{r=r_2} = \left.\frac{\partial \varphi_j^{\mathrm{IV}}(r, \theta)}{\partial r}\right|_{r=r_2}. \tag{24}$$

For the PMs

$r = r_3$ and $\theta \in [-\pi/p_2, \pi/p_2]$:

$$\varphi^{\mathrm{I}}(r_3, \theta) = \varphi^{\mathrm{II}}(r_3, \theta) \tag{25}$$

$$\mu_r \left(\frac{\partial \varphi^{\mathrm{I}}}{\partial r}\right)\Big|_{r=r_3} - M_r = \mu_r \left(\frac{\partial \varphi^{\mathrm{II}}}{\partial r}\right)\Big|_{r=r_3} \tag{26}$$

$r = r_4$ and $\theta \in [-\pi/p_2, \pi/p_2]$:

$$\varphi^{\mathrm{I}}(r_4, \theta) = 0. \tag{27}$$

IV. Field Solution

A. Field Distribution in Air Gap

The scalar potential in Region II is governed by the Laplace equation given in (11). By separating the variables r and θ, the general solution can be expressed as

$$\varphi^{\mathrm{II}} = \sum_{n=1}^{\infty} \begin{bmatrix} (E_n r^{np_2} + F_n r^{-np_2}) \cos np_2\theta \\ + (G_n r^{np_2} + H_n r^{-np_2}) \sin np_2\theta \end{bmatrix} + E_0 \ln r + G_0 \tag{28}$$

where D_n, E_n, F_n, G_n, D_0, and E_0 are the Fourier coefficients to be determined.

It indicates that the field solutions can be expressed as the sum of several harmonics components around the circumference, and the magnitude of each harmonic is a function of the radial length. It should be noted that the zero harmonic term has to be taken into account. Due to the existence of the FMPs, the magnetic path is no longer even. Thus, the circumferential integration of the scalar magnetic potentials should not be zero. Moreover, considering the periodicity, the zero harmonic term should not be related to θ.

B. Field Distribution in Permanent Magnets

The scalar potential in Region I is governed by the Poisson equation given in (7). According to the superposition law, its general solution is the sum of the solution of the corresponding Laplace equation and one special solution of its own.

First, the general solution of the corresponding Laplace equation is considered. In order to satisfy the boundary conditions given in (25), by using the method of separating variables, the general solution is given by

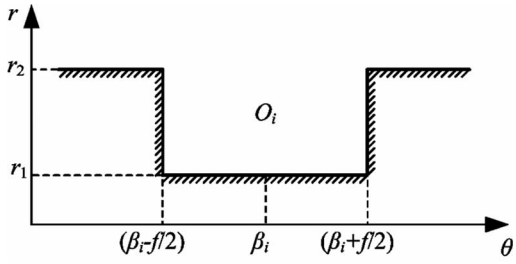

Fig. 4. Region of openings.

$$\varphi_1^{\mathrm{I}} = \sum_{n=1}^{\infty} \begin{bmatrix} (A_n r^{np_2} + B_n r^{-np_2}) \cos np_2\theta \\ + (C_n r^{np_2} + D_n r^{-np_2}) \sin np_2\theta \end{bmatrix} + A_0 \ln r + C_0. \tag{29}$$

Second, the special solution of the Poisson equation is taken into account. The residual magnetization given by (9) and (10) can be rewritten as

$$M_r = \sum_{n=1}^{\infty} M_{rn} \begin{bmatrix} \cos(np_2(\theta_0 + \omega_r t)) \sin np_2\theta \\ -\sin(np_2(\theta_0 + \omega_r t)) \cos np_2\theta \end{bmatrix} \tag{30}$$

$$M_{rn} = \begin{cases} \dfrac{4B_r}{(i\pi\mu_0)}, & \text{when} \quad n = iG_r,\ i = 1, 3, 5, ... \\ 0, & \text{otherwise.} \end{cases} \tag{31}$$

From (7) and (8), it yields

$$\frac{div\left(\vec{M}\right)}{\mu_r} = \frac{M_r}{\mu_r r} + \frac{\partial(M_r)}{\mu_r \partial r} + \frac{\partial(M_\theta)}{\mu_r r \partial\theta} = \frac{M_r}{\mu_r r}. \tag{32}$$

Thus, from (30) to (32), it is easy to find a special solution of (7) given by

$$\varphi_2^{\mathrm{I}} = \sum_{n=1}^{\infty} W_n r \begin{bmatrix} \cos(np_2(\theta_0 + \omega_r t)) \sin np_2\theta \\ -\sin(np_2(\theta_0 + \omega_r t)) \cos np_2\theta \end{bmatrix} \tag{33}$$

$$W_n = \begin{cases} \dfrac{4B_r}{i\pi\mu_0\mu_r\left[1 - (np_2)^2\right]}, & \text{when } n = iG_r,\ i = 1, 3, 5, \ldots \\ 0, & \text{otherwise.} \end{cases} \tag{34}$$

Finally, the general solution of the scalar potential in Region I can be expressed as

$$\varphi^{\mathrm{I}} = \varphi_1^{\mathrm{I}} + \varphi_2^{\mathrm{I}} = \sum_{n=1}^{\infty} \begin{bmatrix} \begin{pmatrix} A_n r^{np_2} + B_n r^{-np_2} \\ -W_n r \sin(np_2(\theta_0 + \omega_r t)) \end{pmatrix} \cos np_2\theta \\ + \begin{pmatrix} C_n r^{np_2} + D_n r^{-np_2} \\ +W_n r \cos(np_2(\theta_0 + \omega_r t)) \end{pmatrix} \sin np_2\theta \end{bmatrix} + A_0 \ln r + C_0 \tag{35}$$

where A_n, B_n, C_n, D_n, A_0, and C_0 are the Fourier coefficients to be determined.

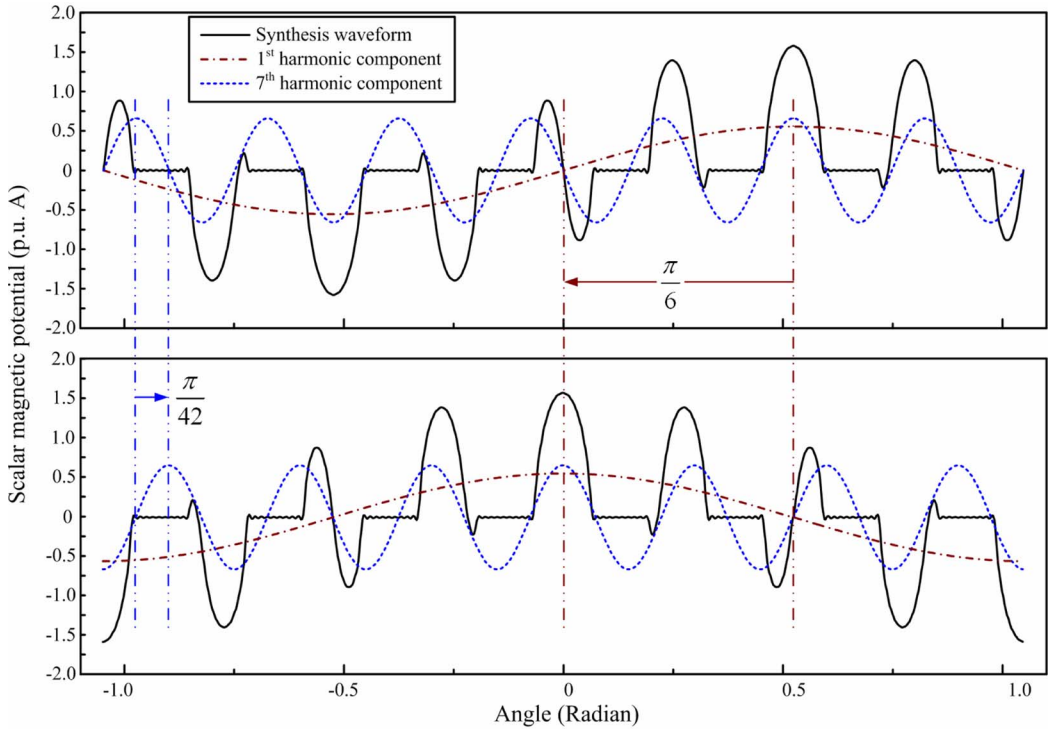

Fig. 5. Scalar magnetic potential distribution on surface of FMPs. From top to bottom: initial phase angle $\theta_0 = 0$ and $\theta_0 = \pi/42$.

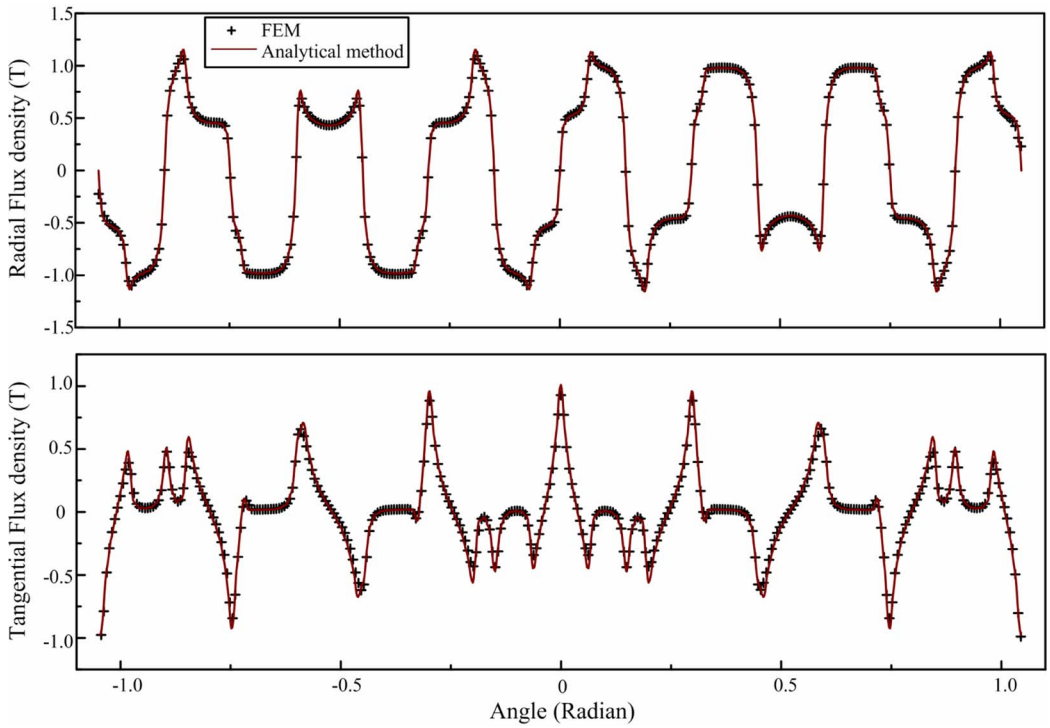

Fig. 6. Magnetic flux density in middle of air gap. From top to bottom: radial component and tangential component.

C. Field Distribution in Opening O_i

Fig. 4 shows the detailed scheme of the region of opening. The scalar potential in the ith opening O_i is governed by the Laplace equations given in (12). Considering the boundary conditions listed in (17) and (18), its general solution should be expressed as

$$\varphi_i^{\mathrm{III}} = \sum_{m=1}^{\infty} \left[\left(I_{im} r^{\lambda_{mf}} + J_{im} r^{-\lambda_{mf}} \right) \sin \lambda_{mf} \left(\theta - \beta_i + \frac{f}{2} \right) \right] \tag{36}$$

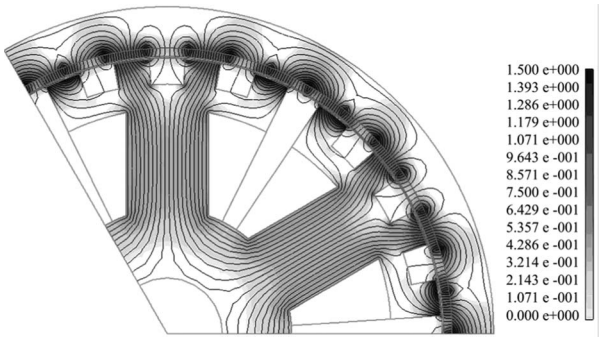

Fig. 7. Flux line distribution.

where $\lambda_{mf} = m\pi/f$, and I_{im} and J_{im} are the Fourier coefficients to be determined.

D. Field Distribution in Slot S_j

The scalar potential in the jth slot S_j is governed by the Laplace equations given in (13). Similar to the case of openings, it is easy to know that the general solution could be expressed as

$$\varphi_j^{\mathrm{IV}} = \sum_{m=1}^{\infty} \left[K_{jm} r^{\lambda_{mg}} \sin \lambda_{mg} \left(\theta - \gamma_j + \frac{g}{2} \right) \right] \tag{37}$$

where $\lambda_{mg} = m\pi/g$, and K_{jm} is the Fourier coefficients to be determined. The reason why only the positive exponential term is employed lies in the assumption on the infinite depth of slots.

E. Boundary Conditions

In what follows, the boundary conditions are discussed so as to determine the parameters defined in the solutions.

First, at the bottom surface of the ith opening O_i ($r = r_1$), from (16) and (36), it yields

$$I_{im} r_1^{\lambda_{mf}} + J_{im} r_1^{-\lambda_{mf}} = 0. \tag{38}$$

Second, on the outside surface of the PMs ($r = r_4$), from (27) and (35), it yields

$$A_0 \ln r_4 + C_0 = 0 \tag{39}$$

$$A_n r_4^{np_2} + B_n r_4^{-np_2} - W_n r_4 \sin\left(np_2\left(\theta_0 + \omega_r t\right)\right) = 0 \tag{40}$$

$$C_n r_4^{np_2} + D_n r_4^{-np_2} + W_n r_4 \cos\left(np_2\left(\theta_0 + \omega_r t\right)\right) = 0. \tag{41}$$

Third, on the inside surface of the PMs ($r = r_3$), from (25), (26), (28), and (35), it yields

$$A_0 \ln r_3 + C_0 = E_0 \ln r_3 + G_0 \tag{42}$$

$$A_n r_3^{np_2} + B_n r_3^{-np_2} - W_n r_3 \sin\left(np_2\left(\theta_0 + \omega_r t\right)\right) = E_n r_3^{np_2} + F_n r_3^{-np_2} \tag{43}$$

$$C_n r_3^{np_2} + D_n r_3^{-np_2} + W_n r_3 \cos\left(np_2\left(\theta_0 + \omega_r t\right)\right) = G_n r_3^{np_2} + H_n r_3^{-np_2} \tag{44}$$

$$A_0 = E_0 \tag{45}$$

$$A_n r_3^{np_2} - B_n r_3^{-np_2} - E_n r_3^{np_2} + F_n r_3^{-np_2} = \left(W_n - \frac{M_{rn}}{\mu_r} \right) \frac{r_3}{np_2} \sin\left(np_2\left(\theta_0 + \omega_r t\right)\right) \tag{46}$$

$$C_n r_3^{np_2} - D_n r_3^{-np_2} - G_n r_3^{np_2} + H_n r_3^{-np_2} = \left(\frac{M_{rn}}{\mu_r} - W_n \right) \frac{r_3}{np_2} \cos\left(np_2\left(\theta_0 + \omega_r t\right)\right). \tag{47}$$

Fourth, on the surface of the FMPs ($r = r_2$), from (20), (21), and (23), the scalar potential on this surface can also be expressed as

$$\varphi^{\mathrm{II}}(r_2,\theta) = \begin{cases} \varphi_1^{\mathrm{IV}}(r_2,\theta), & -\pi/p_2 \le \theta < -\pi/p_2 + g/2 \\ 0, & \alpha_i - e/2 \le \theta < \alpha_i + e/2 \\ \varphi_i^{\mathrm{III}}(r_2,\theta), & \beta_i - f/2 \le \theta < \beta_i + f/2 \\ \varphi_2^{\mathrm{IV}}(r_2,\theta), & -g/2 \le \theta < g/2 \\ \varphi_1^{\mathrm{IV}}(r_2,\theta), & \pi/p_2 - g/2 \le \theta < \pi/p_2. \end{cases} \tag{48}$$

Expanding (48) into Fourier series over $[-\pi/p_2, \pi/p_2]$, one gets

$$\varphi^{\mathrm{II}}(r_2,\theta) = \frac{E_0'}{2} + \sum_{n=1}^{\infty} \left[E_n' \cos\, np_2\theta + G_n' \sin\, np_2\theta \right] \tag{49}$$

$$E_0' = \frac{p_2}{\pi} \int_{-\pi/p_2}^{\pi/p_2} \varphi^{II}(r_2,\theta) d\theta = \frac{p_2}{\pi} \sum_{m=1}^{\infty} \left[\frac{1-(-1)^m}{m\pi} \left(g r_2^{\lambda_{mg}} \sum_{j=1}^{2} K_{jm} + f r_2^{\lambda_{mf}} \sum_{i=1}^{6} I_{im} + f r_2^{-\lambda_{mf}} \sum_{i=1}^{6} J_{im} \right) \right] \tag{50}$$

$$E_n' = \frac{p_2}{\pi} \int_{-\pi/p_2}^{\pi/p_2} \varphi^{II}(r_2,\theta) \cos\, np_2\theta\, d\theta = \frac{p_2}{\pi} \left[\sum_{i=1}^{6} \sum_{m=1}^{\infty} \tau(m,n,f,i,\beta) \left(I_{im} r_2^{\lambda_{mf}} + J_{im} r_2^{-\lambda_{mf}} \right) + \sum_{j=1}^{2} \sum_{m=1}^{\infty} \tau(n,m,g,j,\gamma) K_{jm} r_2^{\lambda_{mg}} \right] \tag{51}$$

$$G_n' = \frac{p_2}{\pi} \int_{-\pi/p_2}^{\pi/p_2} \varphi^{II}(r_2,\theta) \sin\, np_2\theta\, d\theta = \frac{p_2}{\pi} \left[\sum_{i=1}^{6} \sum_{m=1}^{\infty} \sigma(m,n,f,i,\beta) \left(I_{im} r_2^{\lambda_{mf}} + J_{im} r_2^{-\lambda_{mf}} \right) + \sum_{j=1}^{2} \sum_{m=1}^{\infty} \sigma(n,m,g,j,\gamma) K_{jm} r_2^{\lambda_{mg}} \right] \tag{52}$$

where $\tau(\cdot)$ and $\sigma(\cdot)$ are defined by (53) and (54), as shown at the bottom of the next page.

Thus, from (28) and (49), it yields

$$E_0 \ln r_2 + G_0 = E_0' \tag{55}$$

$$E_n r_2^{np_2} + F_n r_2^{-np_2} = E_n' \tag{56}$$

$$G_n r_2^{np_2} + H_n r_2^{-np_2} = G_n'. \tag{57}$$

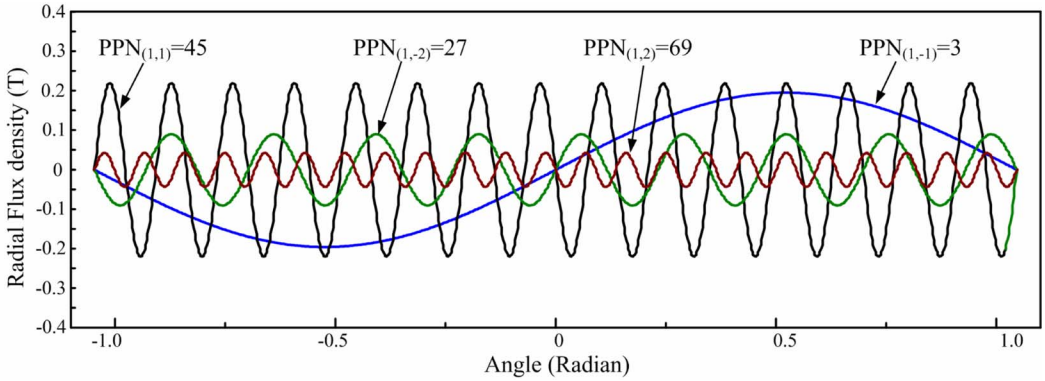

Fig. 8. Asynchronous harmonic components of radial flux density in middle of air gap.

Similarly, from (22), (24), and (49), one gets

$$\frac{E_0(1-(-1)^m)}{\lambda_{mf}}+\sum_{n=1}^{\infty} np_2 \times\left[\begin{array}{l}\tau(m,n,f,i,\beta)\left(E_n r_2^{np_2}-F_n r_2^{-np_2}\right)\\ +\sigma(m,n,f,i,\beta)\left(G_n r_2^{np_2}-H_n r_2^{-np_2}\right)\end{array}\right] = \frac{m\pi}{2}\left(I_{im} r_2^{\lambda_{mf}}-J_{im} r_2^{-\lambda_{mf}}\right) \tag{58}$$

$$\frac{E_0(1-(-1)^m)}{\lambda_{mg}}+\sum_{n=1}^{\infty} np_2 \times\left[\begin{array}{l}\tau(m,n,g,j,\gamma)\left(E_n r_2^{np_2}-F_n r_2^{-np_2}\right)\\ +\sigma(m,n,g,j,\gamma)\left(G_n r_2^{np_2}-H_n r_2^{-np_2}\right)\end{array}\right] = \frac{m\pi}{2} K_{jm} r_2^{\lambda_{mg}}. \tag{59}$$

Consequently, all the Fourier coefficients can be determined by (38)–(47) and (55)–(59). After the scalar potentials in each region are obtained, the flux density can be deduced by

$$B_r = -\mu_0 \frac{\partial \varphi}{\partial r} \tag{60}$$

$$B_\theta = -\mu_0 \frac{1}{r}\frac{\partial \varphi}{\partial \theta} \tag{61}$$

where B_r and B_θ represent the radial and tangential components of the flux density, respectively.

TABLE I
ASYNCHRONOUS HARMONICS

u	v	PPN$_{(u,v)}$	G_r	Magnitude [T]
1	-1	3	-7:1	0.1779
	1	45	7:15	0.1999
1	-2	27	-7:9	0.0820
	2	69	7:23	0.0393
1	-3	51	-9:17	0.0244
	3	93	9:31	0.0634
3	-1	39	21:13	0.0310
	1	87	21:29	0.0360
3	-2	15	21:5	0.0064
	2	111	21:37	0.0023
3	-3	9	-7:1	0.0041
	3	135	7:15	0.0118

V. CALCULATION RESULTS

Fig. 5 shows the scalar potential distribution along the surface of the FMPs ($r = r_2$) with different initial phase angle θ_0. The first harmonic component (PPN = 3) and the seventh harmonic component (PPN = 21) are also shown. It can be found that when the seventh harmonic component moves rightward by $\pi/42$ with the rotor, the first harmonic component will move leftward by $\pi/6$. This agrees well with the magnetic-gearing effect given in (4).

$$\tau(m,n,u,v,\Gamma) = \begin{cases} \dfrac{\lambda_{mu}\left[\cos np_2\left(\Gamma_v-\frac{u}{2}\right)-(-1)^m\cos np_2\left(\Gamma_v+\frac{u}{2}\right)\right]}{\lambda_{mu}^2-(np_2)^2}, & (\lambda_{mu}\neq np_2) \\ \dfrac{\cos np_2\left(\Gamma_v-\frac{u}{2}\right)-(-1)^m\cos np_2\left(\Gamma_v+\frac{u}{2}\right)}{2(\lambda_{mu}+np_2)}+\dfrac{u\sin\left(\frac{m\pi}{2}-\lambda_{mu}\Gamma_v\right)}{2}, & (\lambda_{mu}=np_2) \end{cases} \tag{53}$$

$$\sigma(m,n,u,v,\Gamma) = \begin{cases} \dfrac{\lambda_{mu}\left[\sin np_2\left(\Gamma_v-\frac{u}{2}\right)-(-1)^m\sin np_2\left(\Gamma_v+\frac{u}{2}\right)\right]}{\lambda_{mu}^2-(np_2)^2}, & (\lambda_{mu}\neq np_2) \\ \dfrac{\sin np_2\left(\Gamma_v-\frac{u}{2}\right)-(-1)^m\sin np_2\left(\Gamma_v+\frac{u}{2}\right)}{2(\lambda_{mu}+np_2)}+\dfrac{u\cos\left(\frac{m\pi}{2}-\lambda_{mu}\Gamma_v\right)}{2}, & (\lambda_{mu}=np_2) \end{cases} \tag{54}$$

Fig. 6 shows the magnetic field density in the middle of the air gap. In order to assess the validity of the proposed analytical method, the corresponding results derived from the FEM are provided for comparison. When using the FEM, the calculation zone is divided into 11 320 triangular elements, and then the Newton–Raphson (N–R) method combined with the incomplete Cholesky-conjugate gradient (ICCG) algorithm is used to solve the nonlinear equations. In order to test the infinite permeability assumption, two cases have been taken into consideration: In case 1, the infinite permeability assumption is adopted for the iron yokes. In case 2, the B-H characteristic of the laminated silicon steel (Type 50H470) is engaged for the iron yokes. The calculated results did not show significant difference between these two cases, which demonstrates that the infinite permeability assumption is acceptable in this model. Fig. 7 illustrates the flux line distribution obtained by using the FEM. It can be seen that the analytical results closely agree with the FEM results.

Fig. 8 shows the dominant asynchronous harmonic components of the radial flux density in the middle of the air gap. Their rotational magnitudes and the resulted gear ratios are listed in Table I. It can be found that the first harmonic component ($\mathrm{PPN}_{(1,-1)} = 3$) is of high strength and could result in remarkable speed variation. More importantly, it has the same PPN with the fundamental component of the electromagnetic field excited by the armature windings; thus, stable torque transmission and energy conversion can be achieved through their interaction.

VI. Conclusion

In this paper, an analytical approach to calculate the magnetic field distribution in a low-speed PM harmonic machine is developed. First, the magnetic-gearing effect from which the harmonic machine is derived is discussed. Second, a series-slot model which is composed of a group of partial differential equations concerning the scalar magnetic potential is built up. Third, the field solutions are obtained by using the method of separating variables and analyzing the field boundary conditions. Finally, the flux densities are derived from the scalar potentials. All the results agree well with those obtained from the FEM.

References

[1] J. Chen, C. V. Nayar, and L. Xu, "Design and finite-element analysis of an outer-rotor permanent-magnet generator for directly coupled wind turbines," *IEEE Trans. Magn.*, vol. 36, no. 5, pp. 3802–3809, Sep. 2000.

[2] H. Polinder, F. F. A. Van Der Pijl, G. J. de Vilder, and P. J. Tavner, "Comparison of direct-drive and geared generator concepts for wind turbines," *IEEE Trans. Energy Convers.*, vol. 21, no. 3, pp. 725–733, Sep. 2006.

[3] R. L. Ficheus, F. Caricchi, F. Crescimbini, and O. Honorati, "Axial-flux permanent-magnet motor for direct-drive elevator systems without machine room," *IEEE Trans. Ind. Appl.*, vol. 37, no. 16, pp. 1693–1701, Nov./Dec. 2001.

[4] K. M. Rahman, N. R. Patel, T. G. Ward, J. M. Nagashima, F. Caricchi, and F. Crescimbini, "Application of direct-drive wheel motor for fuel cell electric and hybrid electric vehicle propulsion system," *IEEE Trans. Ind. Appl.*, vol. 42, no. 5, pp. 1185–1192, Sep./Oct. 2006.

[5] P. Kasinathan, A. Grauers, and E. S. Hamdi, "Force density limits in low-speed pm machines due to saturation," *IEEE Trans. Energy Convers.*, vol. 20, no. 1, pp. 37–44, Mar. 2005.

[6] A. Grauers and P. Kasinathan, "Force density limits in low-speed pm machines due to temperature and reactance," *IEEE Trans. Energy Convers.*, vol. 19, no. 3, pp. 518–525, Sep. 2004.

[7] J. Wang, K. Atallah, Z. Q. Zhu, and D. Howe, "Modular three-phase permanent-magnet brushless machines for in-wheel applications," *IEEE Trans. Veh. Technol.*, vol. 57, no. 5, pp. 2714–2720, Dec. 2006.

[8] A. M. El-Refaie and T. M. Jahns, "Analysis of surface permanent magnet machines equipped with concentrated windings," *IEEE Trans. Energy Convers.*, vol. 21, no. 1, pp. 34–43, Mar. 2006.

[9] A. M. El-Refaie and T. M. Jahns, "Impact of winding layer number and magnet type on synchronous surface pm machines designed for wide constant-power speed range operation," *IEEE Trans. Energy Convers.*, vol. 23, no. 1, pp. 53–60, Mar. 2008.

[10] A. M. El-Refaie and T. M. Jahns, "Optimal flux weakening in surface pm machines using fractional-slot concentrated windings," *IEEE Trans. Ind. Appl.*, vol. 41, no. 3, pp. 790–800, May/Jun. 2005.

[11] A. Toba and T. A. Lipo, "Generic torque-maximizing design methodology of surface permanent-magnet vernier machine," *IEEE Trans. Ind. Appl.*, vol. 36, no. 6, pp. 1539–1546, Nov./Dec. 2000.

[12] S. Taibi, A. Tounzi, and F. Piriou, "Study of a stator current excited vernier reluctance machine," *IEEE Trans. Energy Convers.*, vol. 21, no. 4, pp. 823–831, Dec. 2006.

[13] K. Atallah and D. Howe, "A novel high-performance magnetic gear," *IEEE Trans. Magn.*, vol. 37, no. 4, pp. 2844–2846, Jul. 2001.

[14] K. Atallah, S. D. Calverley, and D. Howe, "Design, analysis and realisation of a high-performance magnetic gear," *IEE Proc.—Electric Power Appl.*, vol. 151, no. 2, pp. 135–143, Mar. 2004.

[15] L. Jian and K. T. Chau, "A coaxial magnetic gear with halbach permanent-magnet arrays," *IEEE Trans. Energy Convers.*, vol. 25, no. 2, pp. 319–328, Jun. 2010.

[16] L. Jian, K. T. Chau, and J. Z. Jiang, "A magnetic-geared outer-rotor permanent-magnet brushless machine for wind power generation," *IEEE Trans. Ind. Appl.*, vol. 45, no. 3, pp. 954–962, May/Jun. 2009.

[17] L. Wang, J. Shen, P. Luk, W. Fei, C. Wang, and H. Hao, "Development of a magnetic-geared permanent-magnet brushless motor," *IEEE Trans. Magn.*, vol. 45, no. 10, pp. 4578–4581, Oct. 2009.

[18] W. N. Fu and S. L. Ho, "A quantitative comparative analysis of a novel flux-modulated permanent-magnet motor for low-speed drive," *IEEE Trans. Magn.*, vol. 46, no. 1, pp. 127–134, Jan. 2010.

[19] J. Li, K. T. Chau, J. Z. Jiang, C. Liu, and W. Li, "A new efficient permanent-magnet vernier machine for wind power generation," *IEEE Trans. Magn.*, vol. 46, no. 6, pp. 1475–1478, Jun. 2010.

[20] Z. Q. Zhu and D. Howe, "Instantaneous magnetic field distribution in brushless permanent magnet dc motors, Part III: Effect of stator slotting," *IEEE Trans. Magn.*, vol. 29, no. 1, pp. 143–151, Jan. 1993.

[21] D. Zarko, D. Ban, and T. A. Lipo, "Analytical calculation of magnetic field distribution in the slotted air gap of a surface permanent-magnet motor using complex relative air-gap permeance," *IEEE Trans. Magn.*, vol. 42, no. 7, pp. 1828–1837, Jul. 2006.

[22] T. C. O'Connell and P. T. Krein, "A Schwarz–Christoffel-based analytical method for electric machine field analysis," *IEEE Trans. Energy Convers.*, vol. 24, no. 3, pp. 565–577, Sep. 2009.

[23] A. B. Proca, A. Keyhani, A. EL-Antably, W. Lu, and M. Dai, "Analytical model for permanent magnet motors with surface mounted magnets," *IEEE Trans. Energy Convers.*, vol. 18, no. 3, pp. 386–391, Sep. 2003.

[24] J. Azzouzi, G. Barakat, and B. Dakyo, "Quasi-3-D analytical modeling of the magnetic field of an axial flux permanent-magnet synchronous machine," *IEEE Trans. Energy Convers.*, vol. 20, no. 4, pp. 746–752, Dec. 2005.

[25] L. Jian, K. T. Chau, Y. Gong, J. Jiang, and W. Li, "Analytical calculation of magnetic field in surface-inset permanent magnet motors," *IEEE Trans. Magn.*, vol. 45, no. 10, pp. 4688–4691, Oct. 2009.

[26] Z. J. Liu and J. T. Li, "Accurate prediction of magnetic field and magnetic forces in permanent magnet motors using an analytical solution," *IEEE Trans. Energy Convers.*, vol. 23, no. 3, pp. 717–726, Sep. 2008.

[27] T. Lubin, S. Mezani, and A. Rezzoug, "Exact analytical method for magnetic field computation in the air gap of cylindrical electrical machines considering slotting effects," *IEEE Trans. Magn.*, vol. 46, no. 4, pp. 1092–1099, Apr. 2010.

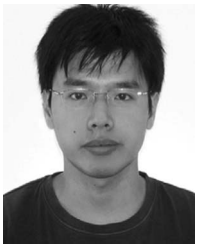

Linni Jian (S'07–M'09) received the B.Eng. degree from the Huazhong University of Science and Technology, Wuhan, China, in 2003, the M.Eng. degree from the Institute of Electrical Engineering, Chinese Academy of Sciences, Beijing, China, in 2006, and the Ph.D. degree from The University of Hong Kong, Pokfulam, Hong Kong, in 2010.

He is currently an Assistant Professor at Shenzhen Institutes of Advanced Technology, Chinese Academy of Sciences. His research interests include the areas of electric drives, electric vehicles, power electronics, and smart grid. In these areas, he has published more than 20 referred technical papers.

Guoqing Xu received the B.Sc., M.Sc., and Ph.D. degrees in electrical engineering from Zhejiang University, Hangzhou, China, in 1988, 1991, and 1994, respectively.

He was a Postdoctoral Researcher with Northern Jiaotong University, Beijing, China. He was with Tongji University, Shanghai, China, where he joined in 1997 as an Associate Professor and Professor in the Department of Electrical Engineering, and was promoted as the Chair of the Department of Electrical Engineering until 2003. From 2006 to 2007, he was a Visiting Professor in the Department of Automation and Computer-Aided Engineering, The Chinese University of Hong Kong (CUHK), Hong Kong,. Since 2007, he has been a Research Professor with the Mechanical and Automation Engineering, CUHK. He has been an Associate Director of CUHK-CAS Shenzhen Institutes of Advanced Integration Technology, CUHK, since 2007. He has been the Chief Scientist of R&D Centre for Electric Vehicle, Chinese Academy of Sciences, China, since 2009. He has also been the Director of CUHK-CAS Shenzhen Institutes of Advanced Integration Technology, CUHK, since 2010. He has published more than 100 referred papers in international journals and conferences. His current research interests include electric vehicle control, energy processing, and automotive electronics.

Chunting Chris Mi (S'00–A'01–M'01–SM'03) received the B.S.E.E. and M.S.E.E. degrees from Northwestern Polytechnical University, Xi'an, China, and the Ph.D. degree from the University of Toronto, Toronto, Ontario, Canada, all in electrical engineering.

He is currently an Associate Professor Electrical and Computer Engineering, and the Director of DTE Power Electronics Laboratory at the University of Michigan-Dearborn, Dearborn. Previously, he was an Electrical Engineer with General Electric Canada, Inc. He has conducted extensive research and published more than 100 articles. His research interests include electric drives, power electronics, electric machines, renewable energy systems, and electrical and hybrid vehicles.

Dr. Mi is the recipient of the National Innovation Award, Government Special Allowance Award, Distinguished Teaching Award, and Distinguished Research Award of the University of Michigan-Dearborn. He is also a recipient of the 2007 IEEE Region 4 Outstanding Engineer Award, the IEEE Southeastern Michigan Section Outstanding Professional Award, and the SAE Environmental Excellence in Transportation (E2 T) Award. He is the Chair of the IEEE Southeastern Michigan Section (2008–2009). He was Vice Chair of the IEEE Southeastern Michigan Section from 2006 to 2007, and Chair in 2008. He was the General Chair of the fifth IEEE Vehicle Power and Propulsion Conference held in Dearborn, in September 6–11, 2009. He is an Associate Editor of the IEEE TRANSACTIONS ON VEHICULAR TECHNOLOGY, an Associate Editor of the IEEE TRANSACTIONS ON POWER ELECTRONICS—LETTERS, a Senior Editor of the IEEE VEHICULAR TECHNOLOGY MAGAZINE, a Guest Editor of the *International Journal of Power Electronics*, an Editorial Board Member of the *International Journal of Electric and Hybrid Vehicles* and *IET Electrical Systems in Transportation*, and an Associate Editor of the *Journal of Circuits, Systems, and Computers* (2007–2009).

K. T. Chau (M'89–SM'04) received the B.Sc.(Eng.) (first-class Hons.), M.Phil., and Ph.D. degrees in electrical and electronic engineering from The University of Hong Kong, Pokfulam, Hong Kong, in 1988, 1991, and 1993, respectively.

He is currently a Professor in the Department of Electrical and Electronic Engineering, and the Director of International Research Center for Electric Vehicles, The University of Hong Kong. His teaching and research interests focus on three main areas: electric vehicles, electric drives, and power electronics. In these areas, he has published more than 200 refereed technical papers. He is also a coauthor of a monograph, *Modern Electric Vehicle Technology* (London, U.K.: Oxford Univ. Press, 2001).

Prof. Chau is a Fellow of the IET. He was the recipients of the Outstanding Young Researcher Award in 2003, the University Teaching Fellowship Award in 2004, and the Award for Innovative Excellence in Teaching, Learning and Technology in 2005.

C. C. Chan (M'77–SM'77–F'92) received the B.Sc., M.Sc., and Ph.D. degrees in electrical engineering from China University of Mining & Technology, Tsinghua University and The University of Hong Kong, in 1957, 1959, and 1982, respectively.

He is currently the Honorary Professor and the former Head of the Department of Electrical and Electronic Engineering, The University of Hong Kong, Pokfulam, Hong Kong. He has had more than ten years industrial experience and more than 35 years academic experience.

He is the Founding President of the International Academy for Advanced Study, China, the Cofounder and Rotating President of the World Electric Vehicle Association, and the President of the Electric Vehicles Association of Asia Pacific. He is a Fellow of the Royal Academy of Engineering, U.K., the Chinese Academy of Engineering, The Ukraine Academy of Engineering Sciences, IEE and HKIE.